Journal of Materials Chemistry A

PAPER

View Article Online
View Journal | View Issue

Cite this: J. Mater. Chem. A, 2017, 5, 2749

Protein-assisted assembly of mesoporous nanocrystals and carbon nanotubes for self-supporting high-performance sodium electrodes†

Guobao Xu,[a] Liwen Yang,*[ab] Zhongyu Li,[a] Xiaolin Wei[a] and Paul K. Chu*[b]

Received 9th November 2016
Accepted 2nd January 2017

DOI: 10.1039/c6ta09673e

www.rsc.org/MaterialsA

Large-scale adoption of sodium-ion batteries in energy storage and conversion devices requires the development of electrode materials with high capacity, high-rate performance and long cycling life. Herein, a self-supporting electrode composed of mesoporous $NaTi_2(PO_4)_3$ nanocrystals and multi-wall carbon nanotubes for Na storage is described. The fabrication process involves protein-assisted self-assembly, a vacuum filtration process, and thermal treatment. The self-supporting electrode possesses favorable features such as hierarchical porosity, interconnected conductive networks, plenty of sites for intercalation-based and interfacial Na storage, and high mechanical robustness, as well as strong synergistic coupling between each constituent. The electrode used directly as the anode in sodium-ion batteries delivers excellent performance such as a high capacity of 132 mA h g^{-1} at 1C, a high initial coulombic efficiency of 99%, and a high-rate capability of 62 mA h g^{-1} at 50C, as well as long-term cycling stability with a capacity of 87% at 10C after 3000 cycles. The freestanding anode possesses favorable properties up to a thickness of 50 μm boding well for a high volumetric/areal capacity. Our study has great potential to be applicable to a wide range of mesoporous nanocrystals of both anodes and cathodes for high-performance energy storage and conversion devices.

1. Introduction

There has been increasing effort to develop sodium ion batteries (SIBs) with a large gravimetric/volumetric capacity, high power density, and long cycling life as alternative large-scale energy storage and conversion (ESC) devices in portable electronics, smart grids, and electric vehicles.[1–6] Unfortunately, the ionic radius of Na^+ is larger than that of Li^+ making it difficult to find appropriate electrode materials with a large tunnel structure and fast ion diffusion pathways enabling stable Na ion extraction and insertion.[7,8] Spherical mesoporous nanocrystals (NCs) with a diameter of about 100 nm have been demonstrated as promising high-performance electrode materials in view of their large surface area, abundant electroactive sites, and alleviation of volume change during charging/discharging, as well as their optimal morphology for compact electrode layers due to their high packing density and good particle mobility, which are desirable in order to attain large volumetric energy and power densities.[9–11] However, the serious concern for this kind of electrode material is the long transport distance of electrons at the sub-micrometer scale.[9] In order to enhance the electron and ion conductivity, one strategy is to construct a three-dimensional (3D) structure comprising mesoporous NCs confined in a highly conductive and interconnected carbon framework such as carbon nanotubes and graphene which also prevents agglomeration of mesoporous NCs during cycling.[10,12,13] In this respect, many types of mesoporous NCs with different surface properties have been prepared[12,14–18] but it is still challenging to achieve effective assembly of mesoporous NCs within an elaborately designed 3D interconnected carbon scaffold.

Owing to their high sodium conductivity, large energy density, excellent thermal stability, and bi-functional properties as both anodes and cathodes, typical compounds with 3D Na super-ionic conductor (NASICON) frameworks such as $Na_3V_2(PO_4)_3$ (NVP) and $NaTi_2(PO_4)_3$ (NTP) have attracted much attention.[5,12,13,19–29] However, the applications of NVP and NTP are hampered by their low capacity and poor high-rate capability as a result of limited chemical diffusion arising from their poor electrical conductivity. Effort to enhance the charge transport kinetics has mainly focused on the use of nanostructured NVP/NTP to reduce electron and Na ion transport lengths and highly conductive carbon to increase surface conductivity and electrical contact in the electrode. For example, Fang *et al.*, reported a hierarchical carbon framework wrapped with NVP NCs with an ultra-long cycling stability of 54% capacity retention after 20 000 cycles at 30C (ref. 13) and Rui *et al.* prepared carbon-coated NVP

[a]Hunan Key Laboratory of Micro-Nano Energy Materials and Devices, School of Physics and Optoelectronics, Xiangtan University, Hunan 411105, China. E-mail: ylwxtu@xtu.edu.cn

[b]Department of Physics and Materials Science, City University of Hong Kong, Tat Chee Avenue, Kowloon, Hong Kong, China. E-mail: paul.chu@cityu.edu.hk

† Electronic supplementary information (ESI) available. See DOI: 10.1039/c6ta09673e

NCs in a porous graphene network with excellent rate capability (86 mA h g^{-1} at 100C) and cycling stability (64% retention after 10 000 cycles at 100C).[24] Wu *et al.* produced a nanocomposite comprising porous NTP NCs embedded in a 3D graphene network with a high rate capability of 67 mA h g^{-1} at 50C, 80% capacity retention after 1000 cycles at 10C, and a high initial coulombic efficiency beyond 79%.[12] Although these nanocomposites possess improved Na storage characteristics, most of them are prepared by the standard but tedious slurry-coating process in the traditional electrode configuration consisting of an electrically insulating polymer binder, conductive additives, and active materials on a metallic current collector foil. Conductive additives and insulating binders not only increase the cost and weight of SIBs, but also adversely affect the electrode performance including the energy and power density per footprint area consequently hampering the application of NTP (or NVP) electrodes in 3D or thin-film batteries.[30,31] Hence, it is highly desirable to develop a new and simple approach to construct self-supporting mixed-conducting nanomaterials to propel direct utilization of hybridized electrodes in high packing-density SIB electrodes.

Herein, the fabrication of a self-supporting electrode consisting of mesoporous NTP (MNTP) NCs confined in a highly conductive and interconnected multi-wall carbon nanotubes (MWCNTs) framework (denoted as MNTP⊂MWCNTs) by a facile method involving protein-assisted self-assembly, vacuum filtration, and thermal treatment is described. In the hierarchical porous architecture, the crosslinked MWCNTs form a robust continuous network enabling rapid electron transport throughout the electrode. The interstitial hierarchical porous channels facilitate electrolyte accessibility thus providing continuous paths for Na transport and the mesoporous framework of MNTP NCs with surrounding pyro-protein provides abundant active sites for sodium intercalation and interfacial Na^+ adsorption. In addition, the hierarchical porous and freestanding architecture prevents self-aggregation among the MNTP NCs and buffers the strain caused by volume change during repetitive Na insertion/extraction resulting in attractive mechanical robustness and improved stability. These favorable features make the self-supporting electrode suitable as a bind-free anode for SIBs with excellent Na^+ storage properties such as a high capacity of 132 mA h g^{-1} at 1C, a high initial coulombic efficiency of 99%, a high-rate capability of 62 mA h g^{-1} at 50C, and long-term cycling stability with a capacity retention of 87% at 10C after 3000 cycles. The self-supporting anode delivers competitive performance up to a thickness of 50 μm.

2. Experimental section

2.1 Materials fabrication

The self-supporting MNTP⊂MWCNTs film was prepared by a modified vacuum filtration process followed by annealing. In the typical process, the crystalline MNTP NCs (about 100 mg) synthesized according to our previous report[32] were dispersed in a solution containing a certain amount (0.5 wt%) of bovine serum albumin (BSA, 96%, Aladdin Industrial Corporation), stirred for 2 h at room temperature, and collected by centrifugation. The BSA-coated MNTP NCs were re-dispersed in deionized water with NH_4HCO_3 (1 mg mL^{-1}), and mixed with a suitable amount of oxidized MWCNTs solution (1 mg mL^{-1}) under continuous stirring for 30 minutes to obtain a homogeneous MNTP NCs/MWCNTs intermediate. The BSA-coated MNTP NCs and MWCNTs were assembled by electrostatic interactions. Subsequently, a black MNTP NCs/MWCNTs intermediate was collected by vacuum filtration using a microporous membrane with a pore size of 0.45 μm and peeled off after drying at 60 °C for 6 h. The product was thermally treated under Ar/H_2 (5%) at 350 °C for 2 h to produce the self-supporting MNTP⊂MWCNTs film. Annealing was performed to form thermally treated BSA and decompose the NH_4HCO_3 in order to enhance the conductivity and robustness of the film. The thickness of the film was controlled by adjusting the content of the vacuum-filtered MNTP NCs/MWCNTs intermediate. A *p*-MNTP/MWCNTs control sample with a similar content of MNTP NCs was prepared by the same procedures but without BSA.

2.2 Materials characterization

The crystal structure was determined by X-ray diffraction (XRD, Rigaku D/max 2500) and the morphology and microstructure were characterized by scanning electron microscopy (SEM) and transmission electron microscopy (TEM, JEOL 2100F) coupled with selected-area electron diffraction (SAED) and Oxford energy-dispersive X-ray spectroscopy (EDS). X-ray photoelectron spectroscopy (XPS) was performed using an Al K_α source (Kratos Analytical Ltd., UK) and the binding energy of 284.8 eV for C 1s was used in the calibration. The nitrogen adsorption–desorption isotherm measurements were conducted at 77 K (Quantachrome NOVA 4000e) and Raman spectra were acquired on a Renishaw inVia system with a $\lambda = 532$ nm laser as the excitation source. Fourier transform infrared (FTIR) spectra were obtained on a FTS-3000 FTIR spectrophotometer. Thermal gravimetric analysis (TGA) and differential scanning calorimetry (DSC) were carried out on a TGA 2050 thermogravimetric analyzer to determine the content of MWCNTs and thermally treated BSA.

2.3 Electrochemical characterization

The electrochemical tests were conducted on two-electrode CR2032 type coin cells. Except for the control electrode which was prepared by mixing the prepared MNTP NCs, super P carbon black, and the PVDF binder at a weight ratio of 70 : 20 : 10 and cast on Cu collectors, the self-supporting MNTP⊂MWCNTs films were directly used as the working electrodes. The coin cells were assembled in an argon-filled glovebox with a metallic sodium foil as the counter electrode and glass fiber (Whatman GF/D) as the separator in the sodium cells. The electrolyte was 1 M $NaClO_4$ in a 1 : 1 (volume) mixture of ethylene carbonate/propylene carbonate. Galvanostatic charging–discharging (GCD) experiments were performed at different current densities in the voltage range between 1.5 and 3 V (*vs.* Na/Na^+) on a multichannel battery testing system (NEWARE BTS-610). Cyclic voltammetry (CV) was performed on an electrochemical workstation (CHI660E) in the voltage range between 1.5 and 3 V (*vs.* Na/Na^+) at different scanning rates and electrochemical impedance

spectroscopy (EIS) was conducted by applying a perturbation voltage of 5 mV in a frequency range of 10^5 to 10^{-2} Hz on the CHI660E electrochemical workstation. The galvanostatic intermittent titration technique (GITT) measurement was programmed by supplying a constant current flux of 0.2C for 10 min followed by an open circuit stand for 80 min, using a cell which previously underwent three discharge–charge cycles.

3. Results and discussion

As illustrated in Fig. 1, the fabrication process of the self-supporting MNTP⊂MWCNTs electrode involves a modified vacuum filtration process followed by annealing during which BSA, an amphiphilic protein with excellent adhesion to solid surfaces *via* hydrophobic and hydrophilic interactions,[33,34] serves as a multifunctional agent to provide good mechanical and electrochemical properties due to engineering interfacial interactions among the nanostructured building units of MNTP NCs and MWCNTs oxidized by nitric acid fumes. The MNTP NCs with high crystallinity, which have a diameter of about 100 nm and a pore size in the range of 1–10 nm as revealed by XRD patterns with Rietveld refinement, TEM, high-resolution TEM (HRTEM), and nitrogen adsorption–desorption isotherm measurements (Fig. S1†), are synthesized hydrothermally and then annealed at 600 °C.[32] The MNTP NCs have abundant –OH groups on their outer surface (absorption between 3000 and 3600 cm^{-1} in the FTIR spectrum in Fig. S2†) which can be grafted with BSA molecules *via* strong hydrophilic (polar) interactions in the dipping process. Under acidic conditions, the BSA-grafted MNTP NCs are positively charged, whereas the MWCNTs oxidized by nitric acid are negatively charged in water on account of ionization of the carboxylic groups and hydroxyl groups.[30,35] The electrostatic interaction between the BSA-grafted MNTP NCs and oxidized MWCNTs leads to the formation of a macroscopically visible MNTP NCs/MWCNTs intermediate that precipitates leaving the solution colorless (Fig. 1). The flocculent MNTP NCs/MWCNTs intermediate is quite stable and there is no MNTP NC precipitate even after several days, implying that the MWCNTs scaffold has a well-defined and interconnected 3D network and the impregnated BSA-grafted NTP mesoporous NCs attach tightly to the MWCNTs (see the right illustration in Fig. 1). Subsequent vacuum filtration and annealing produce the self-supporting MNTP⊂MWCNTs film. The carboxylic groups (–COOH) that bind to the MWCNTs network and MNTP NCs through the interaction between the carboxylic (–COOH) groups in the former and hydroxyl (–OH) groups of the grafted BSA on the latter provide good mechanical integrity after delamination. After annealing at 350 °C, the remaining ammonium salt decomposes without the introduction of other impurities that adversely affect the electrode performance of the free-standing film, while the thermally treated BSA layers on the MWCNTs and MNTP NCs form a cross-linked glue that further prevents the self-supporting film from disintegration, which is obviously different from that observed from the reference sample without the functionalization of BSA (Fig. S3†). Moreover, the dynamic hydrogen bonds between the annealed BSA and MNTP NCs lead to a self-healing effect that allows the reformation of electron conduction paths if the local composite structure is broken.[36] As shown in Fig. 1, the resultant film is mechanically robust (even under bending) and free-standing boding well for direct use in SIB electrodes without binders.

Fig. 2a depicts the typical SEM image of the self-supporting MNTP⊂MWCNTs electrode with a thickness of 25 μm and 40 wt% of MWCNTs. The high-magnification SEM image (Fig. 2b) reveals a porous network consisting of impregnated MNTP NCs and interconnected MWCNTs. No obvious large MNTP NC aggregation can be observed, indicating strong electrostatic interaction between the BSA-grafted MNTP NCs and negatively charged terminated MWCNTs. The TEM and HRTEM images in Fig. 2c and d show the interconnected MWCNTs network and highly dispersed MNTP NCs with a 1.6 nm thick layer of thermally treated BSA (Fig. 2d). The mesoporous characteristic of the MNTP NCs and the (012) plane of the NASICON-type phase with a lattice spacing of 0.61 nm in Fig. S4† confirm the structural conservation of MNTP NCs during the process. Fig. 3 shows the TEM elemental maps revealing homogeneous distributions of carbon and nitrogen in

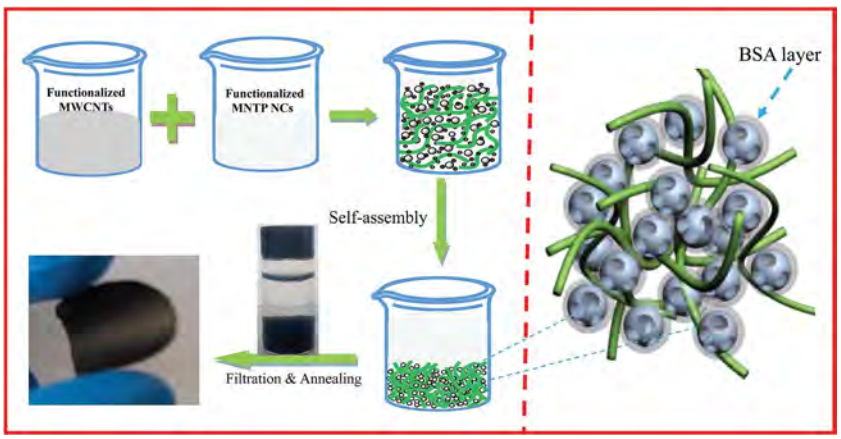

Fig. 1 Schematic illustration of the fabrication of the macroscopically visible assembled MNTP NCs/MWCNTs intermediate and self-supporting MNTP⊂MWCNTs electrodes.

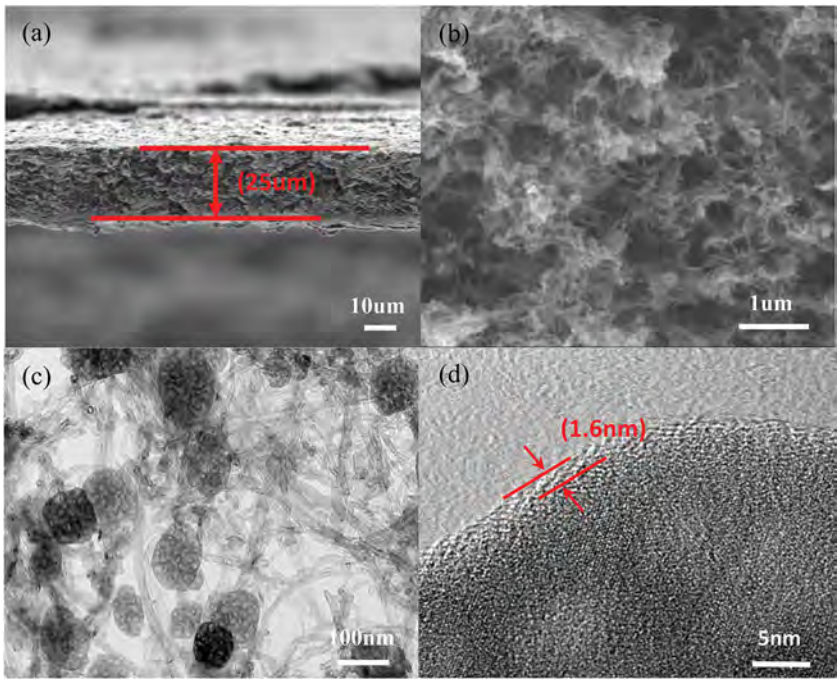

Fig. 2 (a) and (b) Representative SEM images of the self-supporting MNTP⊂MWCNTs electrode. The macropores can be clearly observed; (c) and (d) typical TEM and HR-TEM images of the self-supporting MNTP⊂MWCNTs electrode.

the MWCNTs network and the layer on the MNTP NCs. Fig. 4a shows the typical type-IV isothermal adsorption–desorption curves with a distinct hysteresis loop and a surface area of 88.7 $m^2 g^{-1}$ characteristic of mesoporous materials. The significant nitrogen uptake at a high nitrogen relative pressure over 0.6 suggests good transport properties.[37] Based on the Barrett–Joyner–Halenda model, the self-supporting MNTP⊂MWCNTs electrode exhibits a broad pore size distribution between 2 and 100 nm (see Fig. 4b). The pore size distribution is different from those of MNTP NCs (see Fig. S1†) and the *p*-MNTP/MWCNTs control sample (Fig. S5†),

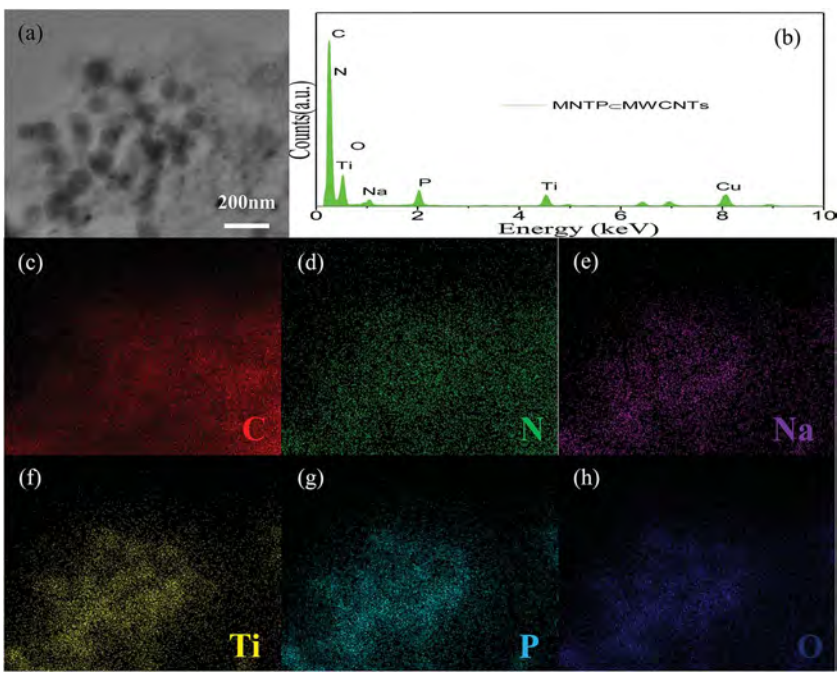

Fig. 3 (a) STEM; (c–h) TEM elemental maps of the self-supporting MNTP⊂MWCNTs electrode; (b) EDS spectrum. The results show the surroundings of the MNTP NCs with homogeneously distributed carbon and nitrogen in the assembled nanocomposite.

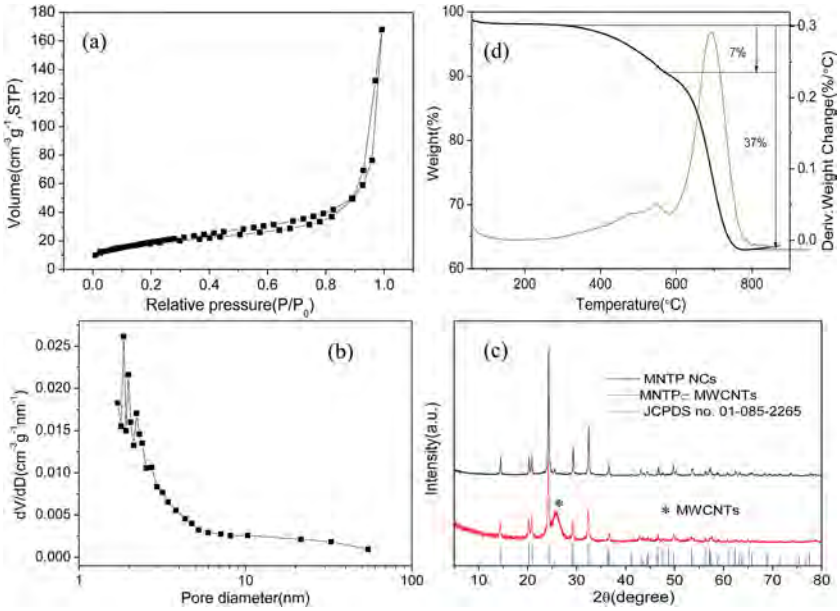

Fig. 4 (a) and (b) Nitrogen-adsorption isotherms and corresponding pore-size distribution of the self-supporting MNTP⊂MWCNTs electrode; (c) XRD patterns of the self-supporting MNTP⊂MWCNTs electrode and reference samples. (d) TGA/DSC curves of the self-supporting MNTP⊂MWCNTs electrode.

suggesting the important influence of thermally treated BSA. Considering the macropores observed from the SEM observations (see Fig. 2b), the results indicate that the self-supporting MNTP⊂MWCNTs electrode possesses a hierarchically porous and interconnected structure with a high surface area.

The structure and composition of the self-supporting MNTP⊂MWCNTs electrode are determined by XRD, Raman scattering, FTIR, XPS, TGA, and DSC. As shown in Fig. 4c, besides the peak at 26.4° associated with the (002) peak of MWCNTs, the other XRD peaks match those of the NASICON-type MNTP NCs (JCPDS no. 01-085-2265). The corresponding TGA/DSC results in Fig. 4d show that the self-supporting MNTP⊂MWCNTs electrode is mainly composed of 63 wt% MNTP and 30 wt% MWCNTs. The mass loss of 7 wt% at below 500 °C stems from the decomposition of thermally treated BSA. The survey and high-resolution Na 1s, Ti 2p, P 2p, O, C 1s and N 1s XPS spectra in Fig. 5a and S6† reveal the presence of Na, Ti, P, O, C, and N. Compared with the results from that of MWCNTs treated under the similar experimental conditions (see Fig. S7†), the nitrogen in the self-supporting MNTP⊂MWCNTs electrode mainly originates from thermally treated BSA. The high-resolution N 1s spectrum in Fig. 5b indicates at least three nitrogen chemical states with the deconvoluted peaks at 398.8 and 399.7 eV ascribed to pyridine and pyridonic nitrogen of the aromatic compound consistent with those observed from silk proteins at 350 °C.[38] The results confirm the existence of thermally treated BSA in the self-supporting MNTP⊂MWCNTs electrode. The peak at 400.9 eV originates from graphitic nitrogen and the large ratio of graphitic nitrogen is expected to improve the electrical conductivity and electron transfer.

Fig. 5c shows the FTIR spectra of the self-supporting MNTP⊂MWCNTs electrode. The bands at 1606 and 3411 cm^{-1} are characteristic of –COOH and –OH hydroxyl groups, respectively, and that at 640 cm^{-1} is associated with the vibration of Ti^{4+}–O^{2-} in TiO_6.[22] The presence of P–O bonds in PO_4 and the stretching of PO_4 are reflected by the bands at 1032 cm^{-1} and 571 cm^{-1}, respectively. Compared to the *p*-MNTP/MWCNTs, there are two obvious differences, one being C=C stretching in the aromatic skeleton at 1580 cm^{-1} corroborating the existence of MWCNTs and the other being the new absorption band at 1720 cm^{-1}. The thermally treated BSA at 350 °C exhibits a strong absorption peak at 1580 cm^{-1} (Fig. S8†), attributable to C=C or C=N skeletal vibrations in aromatic compounds. Owing to the presence of thiol, amine, and imidazole groups in BSA and carboxylic groups (–COOH) in the oxidized MWCNTs, during the heat treatment, the groups may self-react forming ester bonds or react with the hydroxyl (–OH) groups on the MNTP NCs forming anhydride bonds as evidenced by the stretching vibrations in the anhydride and ester bonds between 1700 and 1800 cm^{-1}. The bonds enable crosslinking of the MWCNTs, thermally treated BSA, and MNTP NCs forming a robust 3D network to improve the mechanical properties. FTIR thus confirms the co-existence of MWCNTs and thermally treated BSA in the self-supporting MNTP⊂MWCNTs electrode. Fig. 5d shows the Raman spectra of the self-supporting MNTP⊂MWCNTs and reference samples. The Raman bands at 990 and 1085 cm^{-1} originate from symmetrical and asymmetrical stretchings in the NTP lattice,[39] those at 155 and 272 cm^{-1} are associated with the translational vibration of Ti^{4+}, and those at 306, 341, and 438 cm^{-1} correspond to PO_4^{3-}. Besides the vibration modes observed from the MNTP NCs, the two distinctive carbon peaks at 1350 (D band) and 1580 cm^{-1} (G band) suggest that the MNTP NCs are dispersed in the carbon matrix. Compared to the ratio of the D to G bands ($I_G/I_D = 1.33$)

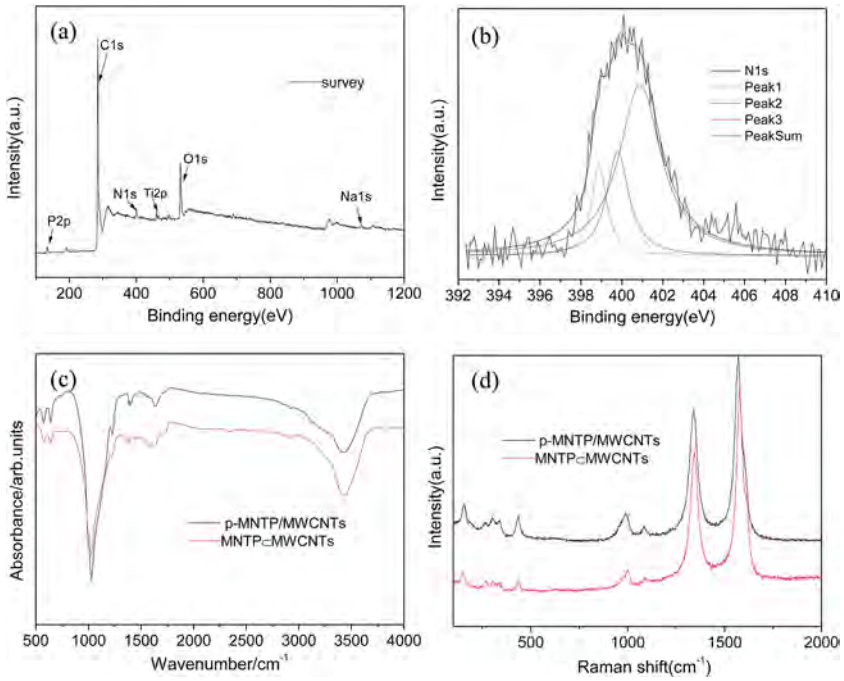

Fig. 5 (a) Survey XPS spectra and (b) high-resolution N 1s spectra acquired from the self-supporting MNTP⊂MWCNTs electrode. (c) and (d) FTIR and Raman spectra of the self-supporting MNTP⊂MWCNTs electrode and reference samples, respectively.

of the reference *p*-MNTP/MWCNTs sample, the ratio of the self-supporting MNTP⊂MWCNTs electrode increases to 1.45, indicating enhanced electron coupling between MNTP NCs and MWCNTs due to cross-linking of the thermally treated BSA[40] consequently resulting in high electrical conductivity.

To investigate the electrochemical properties of the self-supporting MNTP⊂MWCNTs and control electrodes, coin-type cells (CR2032) are fabricated with metallic Na foil as both the counter and reference electrodes. Although the loaded amount of MWCNTs affects the electrochemical performance, it only makes a small contribution to the total capacity (Fig. S9a†). Here, the maximum MNTP NCs content is 71 wt% (Fig. S9b and S9c†). As shown in Fig. S9d,† 40 wt% of MWCNTs is the optimal value for the self-supporting MNTP⊂MWCNTs electrodes. The charging-storage behavior of the self-supporting MNTP⊂MWCNTs electrode with a thickness of 25 μm is evaluated by CV measurement from 1.5 to 3 V for three initial cycles at a scanning rate of 0.5 mV s^{-1} (Fig. 6a). In the first cycle, a single reduction peak at 2.04 V and another peak related to oxidation at 2.3 V corresponding to the redox reaction of Ti^{4+}/Ti^{3+} and the reversible Na^+ insertion–extraction reaction ($NaTi_2(PO_4)_3 + 2Na^+ + 2e^- \leftrightarrow Na_3Ti_2(PO_4)_3$) in the NTP lattice are observed.[12] In the second cycle, the oxidation peak shifts to 2.25 V and the reduction one stays at 2.04 V. The results are similar to those observed from the NTP⊂GN electrode,[12] suggesting stress/strain change around the MNTP NCs due to the formation of the SEI layers.[23] The redox peak positions are almost unchanged during successive scans implying good reversibility. The stable redox polarization is about 0.2 V and comparable to that of the reported NTP⊂GN anode[12] and lower than those of the NTP materials in aqueous and nonaqueous electrolytes,[25,26] indicating a low over potential or less energy necessary for Na^+ insertion into the MNTP NCs. Hence, hybridizing the MNTP NCs with a conductive 3D cross-linked MWCNTs network reduces the resistance for transporting Na^+ and electrons.

Fig. 6b shows the typical GCD profiles acquired from the self-supporting MNTP⊂MWCNTs electrode at a current rate of 1C (1C = 133 mA h g^{-1}) in the voltage range between 1.5 and 3.0 V *vs.* Na/Na^+. There are three regions in the discharging curve including a changing region (I) from the open circuit voltage down to ~2.10 V, a horizontal plateau (II) at ~2.10 V, and another sloping region (III) from 2.10 V down to 1.5 V. The first one arises from a solid solution insertion mechanism and the second one is characteristic of a diffusion-controlled Na^+ intercalation/deintercalation mechanism of NASICON-type NTP. Region III showing a capacity of about 40 mA h g^{-1} (Fig. 6c) reflects a surface process consistent with that of MNTP NCs having a large surface area and a thermally treated BSA coating providing abundant surface sites for fast surface/interfacial sodium reactions. During the charging process, a slope region followed by a plateau at a higher voltage is also observed, indicating a similar sodium-extraction process involving both diffusion and surface processes.[41] Two well-defined and symmetrical voltage plateaus at 2.10 and 2.20 V during discharging and charging can be observed and a small electrochemical polarization of only 100 mV at 1C is observed. The small polarization is almost invariant with cycling (Fig. 6d) and it is different from that of the reference electrode of MNTP NCs mixed with carbon black and the polymer binder [polarization increasing gradually during cycling (Fig. 6e)]. The low and stable electrochemical polarization implies high ion/electron conductivity as a result of the

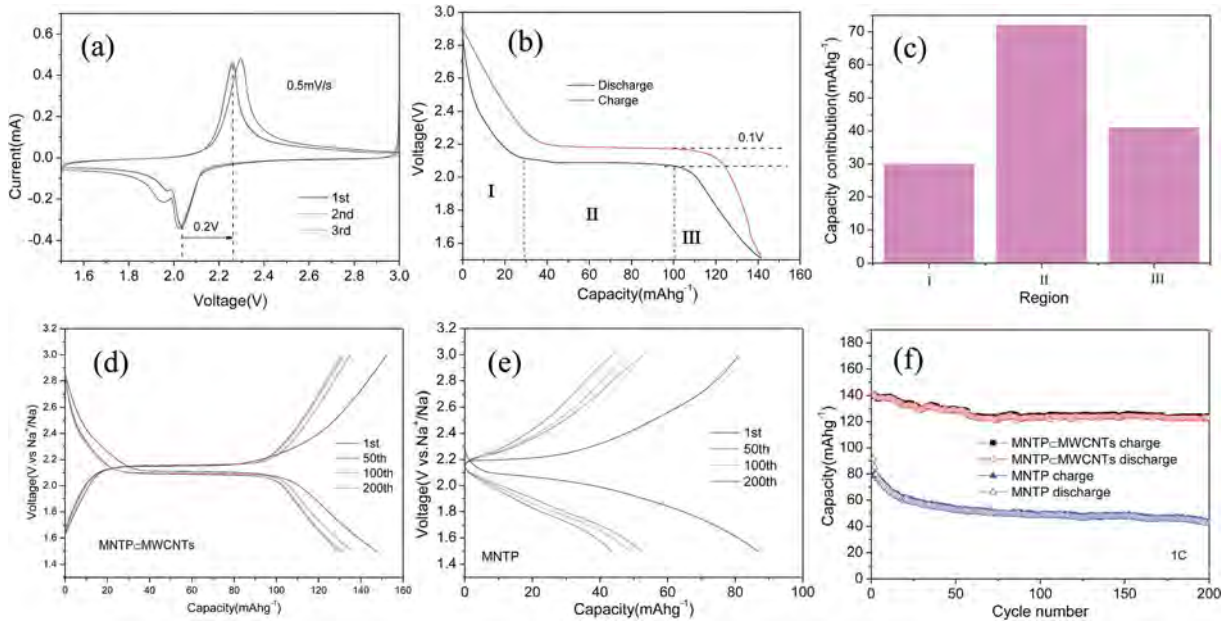

Fig. 6 (a) CV curves of the self-supporting MNTP⊂MWCNTs electrode with a thickness of 25 um for the initial three cycles at a scanning rate of 0.5 mV s^{-1}; (b) typical charge–discharge profiles of the self-supporting MNTP⊂MWCNTs electrode at 1C; (c) capacity contributions from regions I to III marked in (b); (d) and (e) discharge–charge profiles of the self-supporting MNTP⊂MWCNTs electrode and MNTP NCs electrode for the 1st and 200th cycles at a current rate of 1C; (f) cycling performance and coulombic efficiency of the self-supporting MNTP⊂MWCNTs electrode at 1C. The cycling performance of the referenced MNTP NCs electrodes is also shown.

unique hierarchical porous architecture of MNTP NCs confined in 3D MWCNTs networks with thermally treated BSA cross-linking. The initial charging and discharging capacities are 140 and 141 mA h g^{-1}, respectively, corresponding to a coulombic efficiency of 99% which suggests excellent electrochemical reversibility. In fact, the capacity exceeds the theoretical one of NTP (133 mA h g^{-1}) but similar phenomena have been observed from other 3D interconnected carbon nanocomposites such as self-assembled TiO_2–graphene hybrids[10] and graphene-wrapped porous LTO nanofiber composites[42] suggesting additional Na storage at the interfaces of MNTPs/thermally treated BSA and MWCNTs/thermally treated BSA. Fig. 5d shows the cycling performance of the self-supporting MNTP⊂MWCNTs electrode at 1C revealing a reversible capacity as high as 123 mA h g^{-1} and a coulombic efficiency beyond 99% after 200 cycles. In contrast, the reference MNTP NCs exhibit rapid capacity fading with a reversible capacity of 43 mA h g^{-1} after 200 cycles.

Fig. 7a shows the GOD profiles of the self-supporting MNTP⊂MWCNTs electrode with a thickness of 25 μm at different current densities between 0.5 and 50C. The charging–discharging profiles acquired at different current densities have a similar shape consisting of two sloping regions and one plateau region in spite of polarization at a large current density of 50C indicative of better rate capability. As the current increases, the voltage plateau decreases, but the sloping regions do not change, indicating that Na^+ intercalation into the MNTP NCs becomes insufficient at high rates, whereas Na^+ adsorption at the interface (interfacial Na storage) is sufficient even at high rates. The self-supporting MNTP⊂MWCNTs electrode with a thickness of 25 μm shows reversible capacities of 132.8, 126.8, 117.6, 104.9, 91.3, and 81.4 mA h g^{-1} and capacity retention percentages of 97.4%, 93%, 86.2%, 76.9%, 67%, and 59.7% at 1, 2, 5, 10, 20, and 30C, respectively. Even at 50C, a reversible capacity of 64.3 A h g^{-1} is maintained implying rapid charging and discharging within a few minutes at high energy and power densities. The excellent rate performance is comparable to that of recently reported NTP-based nanocomposites.[12,17,19,20,39,43,44] In contrast, the MNTP NC anode shows poor rate characteristics such as a low capacity of 6.7 mA h g^{-1} at 20C due to the absence of a continuous 3D electron/ion conducting network. The relative increase in the discharge capacity is larger at higher rates and the coulombic efficiency at large rates approaches 99% for each cycle indicative of fast Na^+ diffusion and high reversibility. Furthermore, a high capacity of 135.1 mA h g^{-1} can be recovered in subsequent cycling when the current rate is reverted back to 0.5C after the rate capability test, suggesting good structural integrity of the self-supporting MNTP⊂MWCNTs electrode. To further assess the electrochemical performance of the self-supporting MNTP⊂MWCNTs electrode, its cycling performance at a high current rate of 10C is monitored. As shown in Fig. 6c, the electrode at a rate of 10C shows a reversible capacity of 115 mA h g^{-1} in the first cycle and retains a capacity of 100.4 mA h g^{-1} after 3000 cycles with only 0.0042% loss per cycle in addition to a high coulombic efficiency of 99%. To the best of our knowledge, this is the best Na storage performance achieved from self-supporting NTP anodes. The morphology of the self-supporting MNTP⊂MWCNTs electrode after the 3000 cycle tests is depicted in Fig. 7e which shows that the threading MWCNTs and quasi-spherical MNTP NCs are preserved. The crystalline structure of the self-supporting MNTP⊂MWCNTs

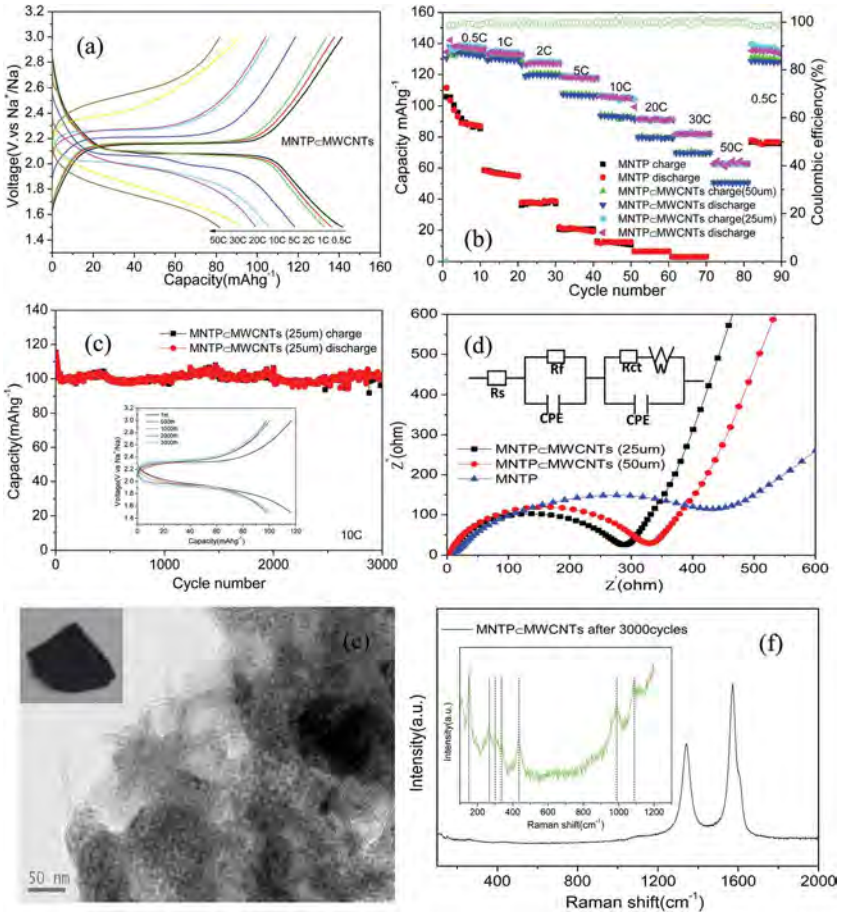

Fig. 7 (a) GCD profiles of the self-supporting MNTP⊂MWCNTs electrode with a thickness of 25 μm at various current rates; (b) rate performance and capacity retention of the MNTP NCs electrode and MNTP⊂MWCNTs electrodes with different thicknesses; (c) cycling performance and GCD profiles (see the inset) of the self-supporting MNTP⊂MWCNTs electrode with a thickness of 25 μm at 10C; (d) Nyquist plots of the MNTP NC, MNTP⊂MWCNTs (25 μm) and MNTP⊂MWCNTs (50 μm) electrodes after the rate capability test. The inset shows the equivalent circuit model, in which R_s, R_f, and R_{ct} are the electrolyte resistance, resistance of the SEI film, and charge transfer resistance, respectively; (e) representative TEM image and photograph (see inset) of the self-supporting MNTP⊂MWCNTs electrode with a thickness of 25 μm after 3000 cycles at 10C; (f) Raman scattering spectra acquired from the self-supporting MNTP⊂MWCNTs electrode with a thickness of 25 μm after 3000 cycles at 10C.

electrode after cycling is investigated by Raman scattering and the results are shown in Fig. 7f. Besides the strong Raman peak from carbon, the characteristic peaks from NASICON-type MNTP NCs are present furnishing evidence about the good structural integrity and cycling stability.

Many battery architectures require the retention of high capacity in spite of a large electrode thickness or areal mass loading, which are crucial to the areal capacity in practice.[45] Hence, the electrochemical sodium storage performance of the MNTP⊂MWCNTs electrode with a thickness of up to 50 μm (Fig. S10†) or twice the areal mass loading is evaluated. As shown in Fig. 7b, at a rate of 50C, the thick electrode still delivers a capacity of 50.6 mA h g^{-1}. The results suggest superior structural uniformity in the thick electrode; otherwise small changes evoking local inhomogeneity can accumulate across the electrode and degrade the electrode performance. Fig. 7d shows the Nyquist plots of the MNTP⊂MWCNTs electrodes based on EIS after the rate capability test. According to the equivalent circuit model in the inset, the charge-transfer resistance (R_{ct}) (Table ESI†) of the self-supporting MNTP⊂MWCNTs is less than that of the MNTP NCs. This is because of the effective electrical contact between the MWCNTs and MNTP NCs in the inter-connected MWCNTs network. The calculated R_{ct} values of the electrodes with thicknesses of 25 μm and 50 μm are 284.7 and 325 Ω, respectively, and the small difference is an indication of the highly effective charge transfer process at the electrode/electrolyte interface and rapid transport kinetics during discharging and charging. In addition, we have performed GITT measurements to determine Na^+ chemical diffusion coefficients and the results are presented in Fig. S11.† The calculated Na^+ chemical diffusion coefficients from the self-supporting MNTP⊂MWCNTs electrodes are comparable, but larger than that from that of MNTP NCs. The results reveal the advantages of a rationally designed hierarchical porous architecture in energy storage applications.

4. Conclusion

A protein-assisted assembling technique to fabricate self-supporting Na electrodes composed of MNTP NCs and MWCNTs is described. The MNTP⊂MWCNTs electrodes are hierarchically porous, highly electrically conductive, and mechanically robust due to their unique architecture in which the mesoporous NCs are confined in the MWCNTs network by pyro-protein cross-linking. The 25 μm thick binder-free electrode has excellent Na^+ storage properties such as a high capacity of 132 mA h g^{-1} at 1C, a high initial coulombic efficiency of 99%, and a high-rate capability of 62 mA h g^{-1} at 50C, as well as a capacity retention of 87% at 10C after 3000 cycles. The 50 μm thick electrode delivers competitive performance as well. Our results reveal a simple and efficient strategy to construct self-supporting composite membranes for high-performance SIBs and it can be extended to other polymers and mesoporous NCs for catalysts, solar cells, and electrochemical energy storage devices.

Acknowledgements

This work was financially supported by grants from the National Natural Science Foundation of China (No. 11474242, 51272220 and 51472209), the Hunan Provincial Innovation Foundation for Graduate (No. CX2016B254), and the City University of Hong Kong Applied Research Grant (ARG) No. 9667122.

References

1 M. Armand and J.-M. Tarascon, *Nature*, 2008, **451**, 652–657.
2 X. Wang, X. Lu, B. Liu, D. Chen, Y. Tong and G. Shen, *Adv. Mater.*, 2014, **26**, 4763–4782.
3 N. Yabuuchi, K. Kubota, M. Dahbi and S. Komaba, *Chem. Rev.*, 2014, **114**, 11636–11682.
4 X. Xiang, K. Zhang and J. Chen, *Adv. Mater.*, 2015, **27**, 5343–5364.
5 S. Guo, J. Yi, Y. Sun and H. Zhou, *Energy Environ. Sci.*, 2016, **9**, 2978–3006.
6 D. Gong, B. Wang, J. Zhu, R. Podila, A. M. Rao, X. Yu, Z. Xu and B. Lu, *Adv. Energy Mater.*, 2016, DOI: 10.1002/aenm.201601885.
7 H. Kim, H. Kim, Z. Ding, M. H. Lee, K. Lim, G. Yoon and K. Kang, *Adv. Energy Mater.*, 2016, **6**, 201600943.
8 G. Xu, L. Yang, X. Wei, J. Ding, J. Zhong and P. K. Chu, *Adv. Funct. Mater.*, 2016, **26**, 3349–3358.
9 H. Liu, Z. Bi, X. G. Sun, R. R. Unocic, M. P. Paranthaman, S. Dai and G. M. Brown, *Adv. Mater.*, 2011, **23**, 3450–3454.
10 S. Yu, L. Yang, Y. Tian, P. Yang, F. Jiang, S. Hu, X. Wei and J. Zhong, *J. Mater. Chem. A*, 2013, **1**, 12750–12758.
11 W. Li, J. Liu and D. Zhao, *Nat. Rev. Mater.*, 2016, **1**, 16023.
12 C. Wu, P. Kopold, Y.-L. Ding, P. A. van Aken, J. Maier and Y. Yu, *ACS Nano*, 2015, **9**, 6610–6618.
13 Y. Fang, L. Xiao, X. Ai, Y. Cao and H. Yang, *Adv. Mater.*, 2015, **27**, 5895–5900.
14 X.-Y. Yu, Y. Feng, Y. Jeon, B. Guan, X. W. Lou and U. Paik, *Adv. Mater.*, 2016, **28**, 9006–9011.
15 Y. Wang, L. Yu and X. W. Lou, *Angew. Chem., Int. Ed.*, 2016, **55**, 7423–7426.
16 X.-Y. Yu, H. B. Wu, L. Yu, F.-X. Ma and X. W. Lou, *Angew. Chem., Int. Ed.*, 2015, **54**, 4001–4004.
17 G. Yang, H. Song, M. Wu and C. Wang, *J. Mater. Chem. A*, 2015, **3**, 18718–18726.
18 L. Yu, H. B. Wu and X. W. D. Lou, *Adv. Mater.*, 2013, **25**, 2296–2300.
19 Y. Fang, L. Xiao, J. Qian, Y. Cao, X. Ai, Y. Huang and H. Yang, *Adv. Energy Mater.*, 2016, **6**, 201502197.
20 J. Yang, H. Wang, P. Hu, J. Qi, L. Guo and L. Wang, *Small*, 2015, **11**, 3744–3749.
21 C. Zhu, K. Song, P. A. van Aken, J. Maier and Y. Yu, *Nano Lett.*, 2014, **14**, 2175–2180.
22 G. Pang, P. Nie, C. Yuan, L. Shen, X. Zhang, H. Li and C. Zhang, *J. Mater. Chem. A*, 2014, **2**, 20659–20666.
23 S. Li, Y. Dong, L. Xu, X. Xu, L. He and L. Mai, *Adv. Mater.*, 2014, **26**, 3545–3553.
24 X. Rui, W. Sun, C. Wu, Y. Yu and Q. Yan, *Adv. Mater.*, 2015, **27**, 6670–6676.
25 W. Wu, A. Mohamed and J. F. Whitacre, *Meet. Abstr.*, 2012, **MA2012–02**, 1859.
26 S. I. Park, I. Gocheva, S. Okada and J.-i. Yamaki, *J. Electrochem. Soc.*, 2011, **158**, A1067–A1070.
27 Q. Li, B. Lin, S. Zhang and C. Deng, *J. Mater. Chem. A*, 2016, **4**, 5719–5729.
28 B. Zhao, B. Lin, S. Zhang and C. Deng, *Nanoscale*, 2015, **7**, 18552–18560.
29 L. Ke, T. Yu, B. Lin, B. Liu, S. Zhang and C. Deng, *Nanoscale*, 2016, **8**, 19120–19128.
30 M. Zhou, X. Li, B. Wang, Y. Zhang, J. Ning, Z. Xiao, X. Zhang, Y. Chang and L. Zhi, *Nano Lett.*, 2015, **15**, 6222–6228.
31 C. Zhu, P. Kopold, P. A. van Aken, J. Maier and Y. Yu, *Adv. Mater.*, 2016, **28**, 2409–2416.
32 G. B. Xu, L. W. Yang, X. L. Wei, J. W. Ding, J. X. Zhong and P. K. Chu, *J. Power Sources*, 2016, **327**, 580–590.
33 J. Liu, S. Fu, B. Yuan, Y. Li and Z. Deng, *J. Am. Chem. Soc.*, 2010, **132**, 7279–7281.
34 Y. J. Yun, W. G. Hong, W.-J. Kim, Y. Jun and B. H. Kim, *Adv. Mater.*, 2013, **25**, 5701–5705.
35 J. Rong, M. Ge, X. Fang and C. Zhou, *Nano Lett.*, 2013, **14**, 473–479.
36 Y. Cheng, Z. Chen, M. Zhu and Y. Lu, *Adv. Energy Mater.*, 2015, **5**, 201401207.
37 J. S. Chen, Y. L. Tan, C. M. Li, Y. L. Cheah, D. Luan, S. Madhavi, F. Y. C. Boey, L. A. Archer and X. W. Lou, *J. Am. Chem. Soc.*, 2010, **132**, 6124–6130.
38 S. Y. Cho, Y. S. Yun, S. Lee, D. Jang, K.-Y. Park, J. K. Kim, B. H. Kim, K. Kang, D. L. Kaplan and H.-J. Jin, *Nat. Commun.*, 2015, **6**, 7145.
39 H.-K. Roh, H.-K. Kim, M.-S. Kim, D.-H. Kim, K. Y. Chung, K. C. Roh and K.-B. Kim, *Nano Res.*, 2016, **9**, 1844–1855.
40 D. V. Kosynkin, A. L. Higginbotham, A. Sinitskii, J. R. Lomeda, A. Dimiev, B. K. Price and J. M. Tour, *Nature*, 2009, **458**, 872–876.
41 Z. Chen, Y. Yuan, H. Zhou, X. Wang, Z. Gan, F. Wang and Y. Lu, *Adv. Mater.*, 2014, **26**, 339–345.

42 C. Chen, H. Xu, T. Zhou, Z. Guo, L. Chen, M. Yan, L. Mai, P. Hu, S. Cheng and Y. Huang, *Adv. Energy Mater.*, 2016, **6**, 201600322.
43 Y. Jiang, L. Zeng, J. Wang, W. Li, F. Pan and Y. Yu, *Nanoscale*, 2015, **7**, 14723–14729.
44 B. Zhao, Q. Wang, S. Zhang and C. Deng, *J. Mater. Chem. A*, 2015, **3**, 12089–12096.
45 Y. Liu, X. He, D. Hanlon, A. Harvey, J. N. Coleman and Y. Li, *ACS Nano*, 2016, **10**, 8821–8828.